Investigation of the uncertainty of initial and boundary conditions in the hindcasts of flow fields over urban areas using a mesoscale numerical weather prediction model

Kawamoto, Yoichi
Faculty of Design, Kyushu University

出版情報：JAPAN ARCHITECTURAL REVIEW. 5 (4), pp.517-529, 2022-09-04. Wiley
バージョン：

Japan Architectural Review
Open Access
Architectural Institute of Japan

Translated Paper

Investigation of the uncertainty of initial and boundary conditions in the hindcasts of flow fields over urban areas using a mesoscale numerical weather prediction model

Yoichi Kawamoto

Faculty of Design, Kyushu University, Fukuoka, Japan

Correspondence
Yoichi Kawamoto, 4-9-1 Shiobaru, Minami-ku, Fukuoka, 815-8540, Japan.
Email: kawamoto@design.kyushu-u.ac.jp

Funding information
Japan Society for the Promotion of Science, Grant/Award Number: JP20K21035

The Japanese version of this paper was published in Volume 87 Number 797, pages 460–471, https://doi.org/10.3130/aije.87.460 of the *Journal of Environmental Engineering* (Transactions of AIJ). The authors have obtained permission for secondary publication of the English version in another journal from the editor of the *Journal of Environmental Engineering* (Transactions of AIJ). This paper is based on a translation of the Japanese version, with slight modifications.

Received July 31, 2022; Accepted August 12, 2022

doi: 10.1002/2475-8876.12282

Abstract

Numerous studies have been conducted using mesoscale numerical weather prediction models to analyze the thermal and wind environments of urban areas around the world. However, weather predictions are highly sensitive to initial conditions. This is the so-called "butterfly effect." In this study, the effects of initial and boundary conditions upon the reproduction accuracy for wind environments (particularly for the sea breeze) over the Fukuoka metropolitan area were investigated by varying (i) the objective analysis data used for the initial and boundary conditions and (ii) the length of the spin-up calculation period. The results of the simulation were compared with surface observations and Doppler LIDAR observations of the airflow field. The accuracy is thought to decrease under an increase in the length of the spin-up calculation period; however, this was not the case in this study. In terms of the differences in the objective analysis data, no clear trend was observed from the comparisons with surface observations; however, slight differences were observed when comparing with the Doppler LIDAR. The lagged average forecasting method (which reduces the uncertainty of the initial conditions by shifting the calculation start time) was also adopted; the ensemble-averaged results showed a good correspondence with the observations.

Keywords
mesoscale numerical weather prediction model, sea breeze, uncertainty, wind environment, WRF

1. Introduction

Numerous studies have employed mesoscale numerical weather prediction models to analyze thermal and wind environments in urban areas. In the field of built environment engineering in Japan, one pioneering study by Mochida et al.[1] analyzed the heat island effect in the Tokyo metropolitan area. Meso-scale numerical weather prediction models have been widely adopted to analyze urban climates worldwide. Kwok and Ng[2] reviewed 102 studies implementing mesoscale numerical weather prediction models for urban climates for the years 2000 to 2019. They reported that the fifth-generation Penn State/NCAR Mesoscale Model (MM5)[3] was most popular (43%) from 2000 to 2010, and the Weather Research and Forecasting (WRF)[4] model was most popular (75%) from 2011 to 2019. The present authors developed an urban canopy model[5–7] that incorporated urban influences into the MM5 land surface model, and they used it to evaluate the heat island effect in the Tokyo metropolitan area, as well as the influence of sea breezes.[8] Observations obtained using Doppler LIDAR and analyses employing the WRF model have also been conducted for sea breeze intrusions in the Fukuoka metropolitan area.[9,10] These studies demonstrate that, in event reproductions targeting a specific day, the accuracy is generally good for thermal environments near the ground surface; however, reproducing the wind environment over an urban area is difficult.

As mentioned above, the aim of conducting numerical calculations using mesoscale numerical weather prediction models

in the fields of built environment engineering and urban climate is not one of forecasting but in most cases rather the reproduction of past events and case studies involving changes in land use or other conditions. In weather forecasting, past event reproduction is called reforecasting or hindcasting, in contrast to real-time forecasting. In this study, re-forecasts and hindcasts were performed using mesoscale numerical weather prediction models and were described as reproducing calculations.

Numerical analyses using numerical weather prediction models suffer from uncertainties attributable to incomplete models or to incomplete initial conditions. Of these uncertainties, this study examines the latter. The fact that small differences in initial conditions can produce large differences in time evolution is referred to as the "sensitivity to initial conditions." In 1963, Lorenz showed via numerical calculations of the Rayleigh–Benard convection that small errors in initial conditions can have a large impact on the predicted results as the time integration progresses.[11] Lorenz also stated that "*If the theory were correct, one flap of a seagull's wings would be enough to alter the course of the weather forever*".[12] The seagull was later replaced by the butterfly, and the phenomena became known as the "butterfly effect," an example of sensitivity to initial conditions.[13]

In the numerical weather-prediction models developed for weather forecasting purposes, the forecast value calculated via a numerical forecast model from the initial conditions at the previous time iteration is used as a first-guess field to create the initial conditions, and data assimilation is applied to modify the first-guess fields using observation data obtained from scattered observation points, to create a three-dimensional spatial distribution of physical quantities. The distribution of created physical quantities is called the analysis data, and data assimilation is also referred to as objective analysis. Owing to the process of data assimilation and the presence of observational errors in the observed values, errors between the real atmosphere and initial conditions obtained from the analysis data are inevitable, making the data incomplete. As a result, uncertainties attributable to the initial conditions are unavoidable. Moreover, while only initial conditions are required for global models that cover the entire Earth, lateral boundary conditions (hereafter referred to as boundary conditions) are also required for mesoscale numerical weather prediction models when the analysis area is limited to a certain region. The boundary conditions can be updated as necessary to incorporate phenomena outside the calculation domain. However, similar to the case for initial conditions, the boundary conditions also contain errors when compared with the real atmosphere; hence, the boundary conditions must also be considered. The objective analysis data used to generate the initial and boundary conditions of mesoscale numerical weather prediction models are provided by meteorological organizations around the world, and it is necessary to consider the accuracy of calculation reproductions obtained using different objective analysis data (i.e., initial and boundary conditions with different error characteristics).

In addition to differences in the initial and boundary conditions, errors are expected to increase over longer analysis periods, because of the sensitivity of the numerical weather prediction model to the initial conditions. However, debate remains regarding the appropriate amount of spin-up calculations for meso-scale numerical weather prediction models. In WRF calculations for meteorology, Skamarock[14] stated that a spin-up of at least 6 to 12 h is necessary, based on a comparison of the kinetic energy spectrum of the free atmosphere (a region of the troposphere above the boundary layer). By comparing temperature and precipitation at 2 m above ground level, Jerez et al.[15] demonstrated that in WRF calculations for climate, a spin-up of approximately 1 week is sufficient; however, if soil temperature and soil moisture are significant, a spin-up of approximately 6 months is required. However, none of these studies have focused on the flow field within the atmospheric boundary layer (particularly in the atmospheric surface layer). Changing the length of the spin-up calculation involves starting the calculation from different initial conditions, which invokes questions regarding both the length of the spin-up calculations and the uncertainty of the initial conditions.

The mesoscale numerical weather prediction model must also consider the impact of the interval required to update the boundary conditions when the calculation period is lengthened. As mentioned above, if phenomena outside the domain can be included in the calculation domain by updating the boundary conditions as required, it should be possible to reproduce the calculations over a long period. In the case of mesoscale forecasts, the boundary conditions are obtained from larger global model forecasts; however, in the reproduction calculations performed in this study, the boundary conditions are generated from objective analysis data; hence, the errors when compared with the real atmosphere are smaller than those of the global model forecasts. If the sensitivities of the initial condition are negligibly small, the influence of the boundary conditions will increase when the calculation period is long, and the differences between the reproduced results will be reduced at reasonably long spin-up calculation periods.

Thus, this study aims to investigate the effects of initial and boundary conditions upon the accuracy of the reproduced wind environment over a city, by varying the objective analysis data used for these conditions and the length of the spin-up calculation. This paper is a reorganization of the content of a paper previously presented at the Annual Conference of the Architectural Institute of Japan,[16–18] with significant additions regarding the calculation target dates and discussions. The Japanese version of this paper was published in Volume 87 Number 797, pages 460–471 (https://doi.org/10.3130/aije.87.460) of the Journal of Environmental Engineering (Transactions of AIJ). The authors have obtained permission for secondary publication of the English version in another journal from the editor of the Journal of Environmental Engineering (Transactions of AIJ). This paper is based on a translation of the Japanese version, with slight modifications.

2. Methods

In this study, to verify the influence of initial and boundary conditions upon the reproducibility of the mesoscale numerical WRF weather prediction model, wind speeds observed via Doppler LIDAR over urban area were compared with those calculated by the WRF model. The following subsections summarize the Doppler LIDAR observations and WRF reproduction calculations.

2.1 Observation of flow fields using doppler LIDAR

Doppler LIDAR LEOSPHERE WINDCUBE v2 was installed at the Ohashi Campus of Kyushu University and used from 9 August to 30 September, 2015 to observe the flow fields over Fukuoka City. The observational data were used to validate the WRF reproduction calculations. The instrument was installed 8 m above ground level, and the wind direction and speed were measured at 12 altitudes (20 m apart, from 48 m

to 268 m above ground level). The observation points are shown in Figure 1. The LEOSPHERE WINDCUBE v2 has a sampling rate of 1 Hz, a wind speed accuracy of 0.1 m/s, a wind speed measurement range of 0–60 m/s, and a wind direction accuracy of 2°.

2.2 Reproduction calculations using the meso-scale numerical WRF weather prediction model

2.2.1 Overview of the WRF model

WRF ver. 3.6.1 was used for reconstruction calculations.

The calculation domains were Domain 1 (3000 km east–west ×2500 km north–south, 25 km horizontal resolution, 75 s time step), Domain 2 (750 × 750 km, 5 km, 15 s), and Domain 3 (240 × 180 km, 1 km, 3 s), as shown in Figure 1. The vertical resolution was identical for Domains 1 to 3 and divided into 45 meshes. In WRF ver. 3.6.1, the vertical direction used the η-coordinate [Note 1], which follows the topography; furthermore, the thickness of each layer in the vertical direction changed according to the time-varying pressure. η was 1 at the ground surface and 0 at the top of the model. The η-coordinates were set at intervals of 0.03 up to the 12th layer above the ground. For the mesh including the Domain 3 Doppler LIDAR observation point, the wind speed definition height of the first layer (from the ground) was ~12.1 m (on average) on the day of analysis; the thickness of the layer near the ground was ~24.2 m. The atmospheric pressure at the top of the calculation domain was set at 100 hPa.

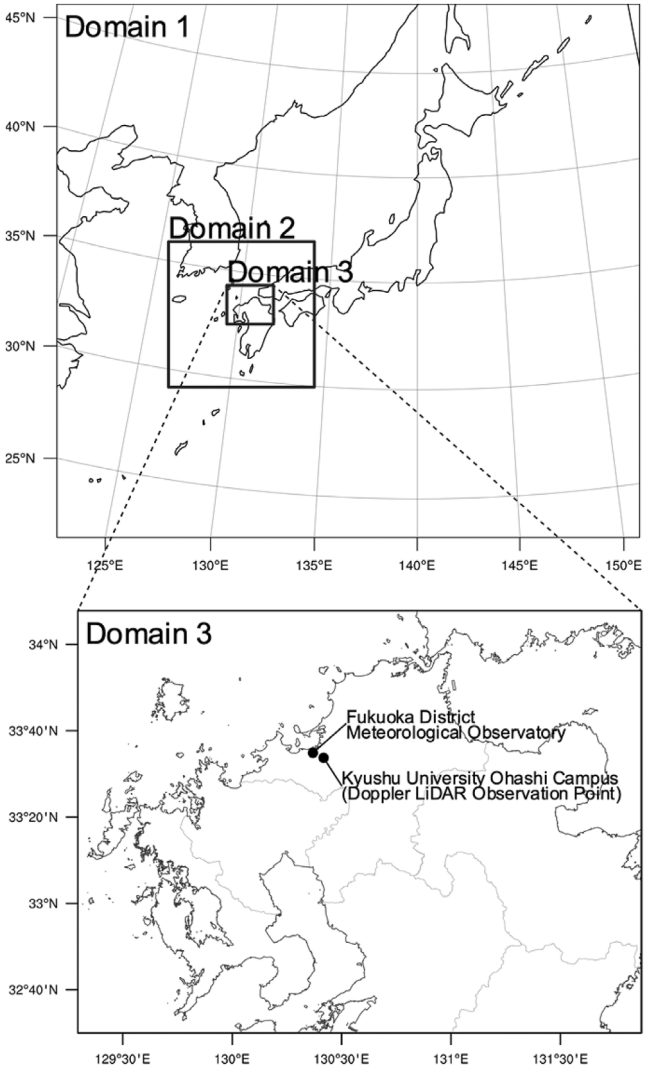

FIGURE 1. WRF calculation domains and observation points

In this study, the following schemes were applied for all domains: The Thompson scheme[19] for cloud microphysics, the Rapid Radiative Transfer Model scheme[20] for longwave radiation, and the Goddard scheme[21] for shortwave radiation. The intervals between the longwave/shortwave radiation calculations were 10 min for Domain 1, 5 min for Domain 2, and 1 min for Domain 3. The Monin–Obukhov (Janjic) scheme[22] was used for the atmospheric surface layer, the Noah land-surface model[23] (LSM) was used for the ground surface (employing the mosaic function), and the Mellor–Yamada–Janjic turbulent kinetic energy scheme[22] was applied for the atmospheric boundary layer. The Grell 3D ensemble scheme[24] was used for cumulus parameterization for Domain 1. The LSM mosaic applied National Land Survey land-use tertiary mesh data (2014), and the number of mosaic categories was set to six. To synchronize the land-use categories of the national land use data to those of the U.S. Geological Survey (USGS) (used in the WRF standard), these categories were reclassified and made to correspond as shown in Table 1, following previous research.[10]

2.2.2 Target dates for reproduction calculations

Fukuoka City faces Hakata Bay, and the influence of sea–land breeze circulation (attributable to the temperature difference between the sea and land surfaces) has a significant impact upon the wind environment. The Fukuoka District Meteorological Observatory (shown in Figure 1) is located ~1 km south of Hakata Bay. According to statistics for the 14 years between 1999 and 2012, the occurrence frequencies for different wind directions at the Fukuoka District Meteorological Observatory were 15.4% north, 14.6% southeast, 12.5% north-northwest, and 9.7% south-southeast throughout the year, with 18.0% north, 14.1% north-northwest, 14.2% southeast, and 10.9% south-southeast winds during the summer, indicating the influence of sea–land breeze circulation. The influence of sea–land breeze circulation is well-established.[25] The target dates for the reproduction calculations were selected to reproduce the temporal changes in wind environment produced by this sea–land breeze circulation.

TABLE 1. Land-use categories in the WRF model, as provided by the National Land Use Data to the U.S. Geological Survey (USGS) and National Land Numerical Information (NLNI) land-use datasets[10]

Land-use categories in WRF (provided by USGS)	Land-use categories in NLNI in 2014
Irrigated Cropland and Pasture	Paddy field
Mixed Dryland/Irrigated Cropland and Pasture	Other agricultural land
Mixed Forest	Forest
Barren or Sparsely Vegetated	Wasteland
	Other land
	Golf course
Urban and Built-up Land	Land for building
	Trunk transportation land (road)
	Trunk transportation land (rail)
Water Bodies	River basin, lake, and marsh
	Beach
	Seawater body

The different characteristics of radiation heating at the sea and land surfaces produce a temperature difference between those surfaces and subsequently a sea–land breeze circulation. Hence, the days with strong solar irradiance were selected as target dates for replication calculations: August 11, 2015, which had the longest period of Doppler LIDAR observations (14 consecutive days without precipitation, including the day under evaluation); August 23, 2015, the largest daily integrated total solar radiation (25.64 MJ); and September 11, 2015, which had the longest sunshine duration (12 h with cloud cover of less than 1 octa for the entire day). Because the sea–land breeze circulation is thought to be driven by small-scale pressure differences and appears clearly when the pressure tilt over a wide area is small, August 15, 2015 was also selected. On that day, the pressure difference at the weather station in northern Kyushu was the smallest, the summed squares of the differences in sea-level pressure in the north–south direction between the Fukuoka District Meteorological Observatory and Kumamoto District Meteorological Observatory, as well as the summed squares of those differences in the east–west direction between the Nagasaki District Meteorological Observatory and Oita District Meteorological Observatory, were calculated. The abovementioned four days were selected for the replication calculations.

2.2.3 Initial and boundary conditions

As discussed in Section 1, the choice of initial and boundary conditions for mesoscale numerical weather prediction models influences the accuracy of the forecast results. In this study, calculations were performed using initial and boundary conditions generated from different objective analysis data, to investigate the influence of the initial and boundary conditions upon the reproduction accuracy. The objective analysis data used were the US National Centers for Environmental Prediction (NCEP) Final (FNL) Operational Global Analysis Data,[26] European Center for Medium-Range Forecasts (ECMWF) ERA-Interim Global Reanalysis Data,[27] and the Japan Meteorological Agency (JMA) Meso-scale Objective Analysis Grid Point Value (GPV). The NCEP FNL use multiple spatial resolutions depending on the time of year; this study used the highest resolution of 0.25° in both latitude and longitude (~27.8 km in the north–south direction and 22.6 km in the east–west direction near Japan), which was made available at 00:00 UTC on July 8, 2015. The ECMWF ERA-Interim is a global reanalysis dataset with a spatial resolution of ~80 km [Note 2]. In operational numerical forecasting, an analysis-forecast cycle is used, for which the analytical value at a certain time is used as the initial condition to run the numerical forecast model and obtain a forecast value, which is subsequently used as the first guess field for analysis at the next initial time, to produce an analytical value via assimilation with the observed data; the numerical forecast model is then run using the analytical value as the initial condition. In this case, time constraints are placed upon the acquisition of observational data that can be used for data assimilation. On the other hand, reanalysis assimilates data from past meteorological events using as many observations as possible; this was carried out in addition to ECMWF ERA-Interim. The JMA Meso-scale Objective Analysis GPV was used for the operational numerical forecast; it has a spatial resolution of 5 km and only covers the area around Japan. The time intervals were 6 h for NCEP FNL and ECMWF ERA-Interim, and 3 h for the JMA Meso-scale Objective Analysis GPV. The initial conditions were obtained from the objective analysis data. However, the JMA Meso-scale Objective Analysis GPV only contains atmospheric data; hence, NCEP FNL was used in combination with soil temperature and other data. Hereafter, the objective analysis data are abbreviated as FNL, ERA, and GPV, respectively.

As mentioned earlier, meso-scale numerical weather prediction models require set boundary conditions to perform calculations. In the WRF model, the outermost domain uses a technique called nudging,[28] by which the outermost grid of the row and column is replaced by a broad-range dataset generated from objective analysis data. The inner four rows and four columns are data assimilation methods that incorporate the forecast values as external force terms, to reduce the difference between the forecast and objective analysis values. In the case of mesoscale forecasts, boundary conditions are created from the global forecast values and used for periodic nudging, which facilitates the reproduction of changes in the pressure field outside the calculation domain, which cannot be reproduced by mesoscale numerical weather prediction models alone. On the other hand, the objective of this study is to reproduce calculations, and the use of objective analysis data for boundary conditions after the start of calculations will facilitate long-term reproduction. In this study, side boundary conditions were created from the objective analysis data used to create the initial conditions, and nudging of the lateral boundary condition was performed every 6 h.

2.2.4 Calculation period

In this study, the effect of the spin-up calculation length upon the reproduced flow field over an urban area was also investigated. Each calculation started at 00:00 UTC (09:00 JST; thereafter, time is expressed as Japan Standard Time) and was performed for the four target days described in Section 2.2.2. The calculations were performed for 1 d and 15 h (15 h of spin-up calculation and 1 d of reproduction calculation), 2 days and 15 h (1 d and 15 h of spin-up calculation and 1 d of reproduction calculation, the same below), 3 days and 15 h, 5 days and 15 h, 7 days and 15 h, 10 days and 15 h, 20 days and 15 h, and 30 days and 15 h; then, the results of the final day's calculation were used for evaluation. The 0.25° NCEP FNL was launched on 8 July, 2015; hence, a period of 60 days and 15 h only was calculated on 11 September, 2015. The respective calculation periods are henceforth abbreviated as 01d15h and so on. The JMA classifies forecasts of 3 h to 2 d as short-range forecasts, those of 2 to 7 d as medium-range forecasts, and those exceeding 7 d as long-range forecasts. Accordingly, 01d15h is a short-range forecast, 02d15h–05d15h are medium-range forecasts, and 7d15h and beyond are long-range forecasts. The shortest forecast, 01d15h, had the same calculation period as the JMA meso-numerical forecast.

3. Results and Discussion

The accuracy of the WRF reproduction was verified. Each calculation result was abbreviated as "FNL_01d15h" or similar, depending on the combination of objective analysis data and calculation period.

It is not possible to show all the results, owing to space limitations; hence, all calculated and observed data and the script used to create the graphs are available on GitHub (https://github.com/yoichi-kawamoto/lidar-wrf-comparison).

3.1 Comparison with ground observations

Among the results of the reproduction calculations, sea-level pressure and wind speed were compared with observations made at the Fukuoka District Meteorological Observatory. Sea level

pressure and wind speed affect the accuracy of sea–land breeze circulation reproduction. The WRF outputs used for comparison were the wind speed 10 m above ground level (calculated from the u- and v-components at that altitude) and sea-level corrected pressure (calculated from the air temperature and mixing ratio 2 m above ground level, the surface pressure, and altitude). Wind speed was not corrected by altitude. The time interval was 10 min. Sea-level pressure was an instantaneous value, and wind speed was a scalar-averaged value.

Table 2 shows the minimum and maximum values of Pearson's correlation coefficient (hereafter referred to as the correlation coefficient) and root mean square error (RMSE) between the calculated and observed sea level pressures for each day of the reproduction calculation. The minimum and maximum values are shown for each objective analysis data point, and the calculation period is shown in brackets. The closer the correlation coefficient is to 1, the better the calculated value captures the changing trend of the observed values; furthermore, the closer the RMSE is to 0, the smaller the error.

The results for 11 and 15 August show that for both objective analysis datasets, cases with short calculation periods (e.g., 01d15h and 02d15h) often have the largest correlation coefficient and the smallest RMSE. On the other hand, the results for 30d15h (which involved a longer calculation) did not necessarily exhibit the lowest correlation coefficient and highest RMSE, and the accuracy of reproduction did not uniformly decrease as the calculation period lengthened. On 23 August, differences in the characteristics were observed for each objective analysis of the data. In contrast, in the ERA case, 01d15h had the lowest correlation coefficient and 30d15h (the longest calculation period) had the highest. In the GPV case, 01d15h had the lowest correlation coefficient and 20d15h had the highest. The maximum RMSE was 01d15h for the ERA and 02d15h for the GPV, with a large error in the case of the shortest calculation period. The reason for this is that the initial values of 01d15h include Typhoons No. 15 and No. 16 in the analysis domain, and the accuracy of the reconstruction of these typhoons differs for each objective analysis; this difference may be reflected in the accuracy of the reproduction calculation. On 11 September, several cases with negative correlation coefficients were noted, with a lowest value of −0.53 for GPV_05d15h. In particular, at 05d15h, when the calculation started at 09:00 (JST) on 5 September, the correlation coefficient was negative and the RMSE was maximum for all objective analysis data. Conversely, in both objective analysis datasets, 01d15h had the largest correlation coefficient and smallest RMSE. A low-pressure system and a frontal system passed over northern Kyushu between 5 and 7 September, and Typhoon No. 18 made landfall in Ehime Prefecture on 9 September. The inability to accurately reproduce these pressure patterns is thought to be the cause of these errors.

Table 3 shows the minimum and maximum values of the correlation coefficients and RMSE between the calculated and observed wind speeds for each day of the reproduced calculations.

In particular, the calculations for 11 September were affected by the sharp drop in the accuracy of the sea-level pressure calculation at 05d15h, as mentioned above. For wind speed, the RMSE at 05d15h was the largest in the calculated results for any objective analysis data. The correlation coefficient was the lowest at 05d15h in the reproduced calculations obtained using the ERA and GPV.

Figure 2 shows the time series graphs of the observed and calculated wind speeds on 11 September, when the RMSE of the wind speed was maximal. In both cases using the objective

TABLE 2. Correlation coefficient and root mean square error (RMSE) for sea level pressure

	Correlation Coefficient						RMSE					
	FNL		ERA		GPV		FNL		ERA		GPV	
Date	Min.	Max.	Min.	Max.	Min.	Max.	Min.	Max.	Min.	Max.	Min.	Max.
8–11	0.30 (03d15h)	0.85 (10d15h)	0.84 (07d15h)	0.93 (01d15h)	0.78 (10d15h)	0.89 (02d15h)	0.37 (10d15h)	0.85 (01d15h)	0.55 (01d15h)	1.75 (05d15h)	0.47 (01d15h)	1.35 (03d15h)
8–15	0.51 (03d15h)	0.86 (02d15h)	0.45 (05d15h)	0.87 (01d15h)	0.44 (20d15h)	0.87 (01d15h)	0.36 (01d15h)	0.69 (03d15h)	0.28 (01d15h)	0.93 (02d15h)	0.71 (03d15h)	0.94 (30d15h)
8–23	0.67 (03d15h)	0.80 (01d15h)	0.72 (01d15h)	0.87 (30d15h)	0.72 (01d15h)	0.80 (20d15h)	0.31 (01d15h)	0.83 (03d15h)	0.38 (02d15h)	0.75 (01d15h)	0.28 (30d15h)	0.39 (02d15h)
9–11	−0.15 (05d15h)	0.90 (01d15h)	−0.45 (05d15h)	0.94 (01d15h)	−0.53 (05d15h)	0.92 (01d15h)	0.68 (01d15h)	3.64 (05d15h)	0.46 (01d15h)	2.97 (05d15h)	0.50 (01d15h)	4.68 (05d15h)

TABLE 3. Correlation coefficient and root mean square error (RMSE) for wind speed

	Correlation Coefficient						RMSE					
	FNL		ERA		GPV		FNL		ERA		GPV	
Date	Min.	Max.	Min.	Max.	Min.	Max.	Min.	Max.	Min.	Max.	Min.	Max.
8–11	0.80 (10d15h)	0.93 (02d15h)	0.66 (03d15h)	0.92 (01d15h)	0.58 (10d15h)	0.91 (03d15h)	0.84 (01d15h)	1.80 (07d15h)	1.14 (01d15h)	1.84 (10d15h)	1.04 (01d15h)	1.79 (03d15h)
8–15	0.55 (10d15h)	0.89 (02d15h)	0.67 (20d15h)	0.89 (01d15h)	0.66 (10d15h)	0.88 (02d15h)	0.81 (02d15h)	1.43 (20d15h)	0.87 (01d15h)	1.44 (05d15h)	0.75 (03d15h)	1.50 (30d15h)
8–23	0.87 (20d15h)	0.94 (05d15h)	0.90 (20d15h)	0.94 (02d15h)	0.89 (20d15h)	0.95 (01d15h)	0.63 (05d15h)	1.28 (02d15h)	0.68 (03d15h)	1.21 (01d15h)	0.63 (07d15h)	0.98 (01d15h)
9–11	0.06 (10d15h)	0.93 (01d15h)	0.17 (05d15h)	0.94 (01d15h)	–0.11 (05d15h)	0.88 (01d15h)	0.60 (01d15h)	4.99 (05d15h)	0.55 (01d15h)	5.02 (05d15h)	1.17 (02d15h)	6.84 (05d15h)

analysis data, the wind speed tended to be overestimated in the morning when the analysis period exceeded 05d15h. This may be because of the accuracy of the pressure-field reproduction, as mentioned earlier.

In the following sections, the wind speeds are compared with observations obtained using Doppler LIDAR for 23 August (when the ranges of minimum and maximum values for the correlation coefficient and RMSE were smallest) and 11 September, when the range of maximum values was the largest.

3.2 Comparison with doppler LIDAR observations

3.2.1 Flow fields on 23 august, 2015

The height of the atmospheric surface layer below the atmospheric boundary layer is generally considered to be ~50 m or 100 m; hence, a comparison was made between the observed and calculated values at a height of 88 m above ground level (i.e., less than 100 m) for the altitudes that were observed by Doppler LIDAR and lay closest to the altitude of the WRF reproduction calculation. The calculated value was in the fourth layer from the ground in the WRF model. The Doppler LIDAR observation site is located to the south-east of Hakata Bay and the sea breeze direction is north-west.

Figure 3 shows the daily variation of the observed and calculated values for wind direction and wind speed at a height of 88 m above ground level on 23 August, 2015. The mean height of the WRF model was 85.0 m. Wind speed was calculated using a 10-min scalar average, and wind direction was calculated using a 10-min unit vector average. The calculated values of the WRF were not corrected for altitude.

The Doppler LIDAR data showed that the wind direction was unstable in the morning; however, from around 11:40, the wind direction stabilized to the northwest, which is the sea breeze; thus, it can be judged that the sea breeze entered the area. The WRF calculation results failed to reproduce the observed wind direction variation during the morning hours (when the wind direction was unstable), although the trends differed depending on the objective analysis data and calculation period. In addition, many reproduction calculations overestimate the wind speed. On the other hand, once the sea breeze started to enter the area, the wind direction was reproduced relatively well in the calculations, though variations in the wind speed reproduction results arose depending on the objective analysis data and calculation period. As a general trend for each objective analysis data point, FNL (red line) and GPV (green line) tended to underestimate the wind speed following the entry of the sea breeze.

As described in Section 2.2.2., this study focuses on changes in the flow field (attributable to sea-land breeze circulation) over an urban area. For sea breezes during the day, it is important to reproduce the time of entry and wind speed. To compare the accuracy of the sea breeze wind speed reproduction, a vertical profile of the wind speed is shown in Figure 4 for 13:50, when the daily maximum wind speed (as observed by the Doppler LIDAR at 88 m above ground level) was 7.17 m/s. The vertical profiles are shown for each objective analysis. As mentioned earlier, the calculation results using FNL and GPV also tended to underestimate the vertical profiles of wind speeds, and the tendency to underestimate the profiles became stronger as the calculation period increased. In contrast, the calculation results using the ERA generally agreed with the observed values and exhibited the smallest variation between calculation periods.

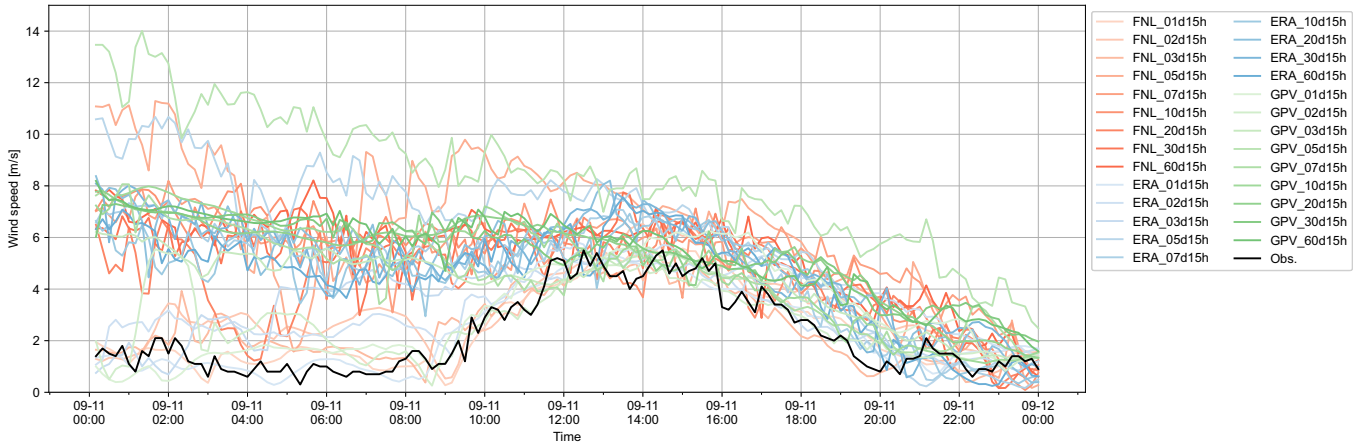

FIGURE 2. Wind speed at the Fukuoka District Meteorological Observatory on September 11

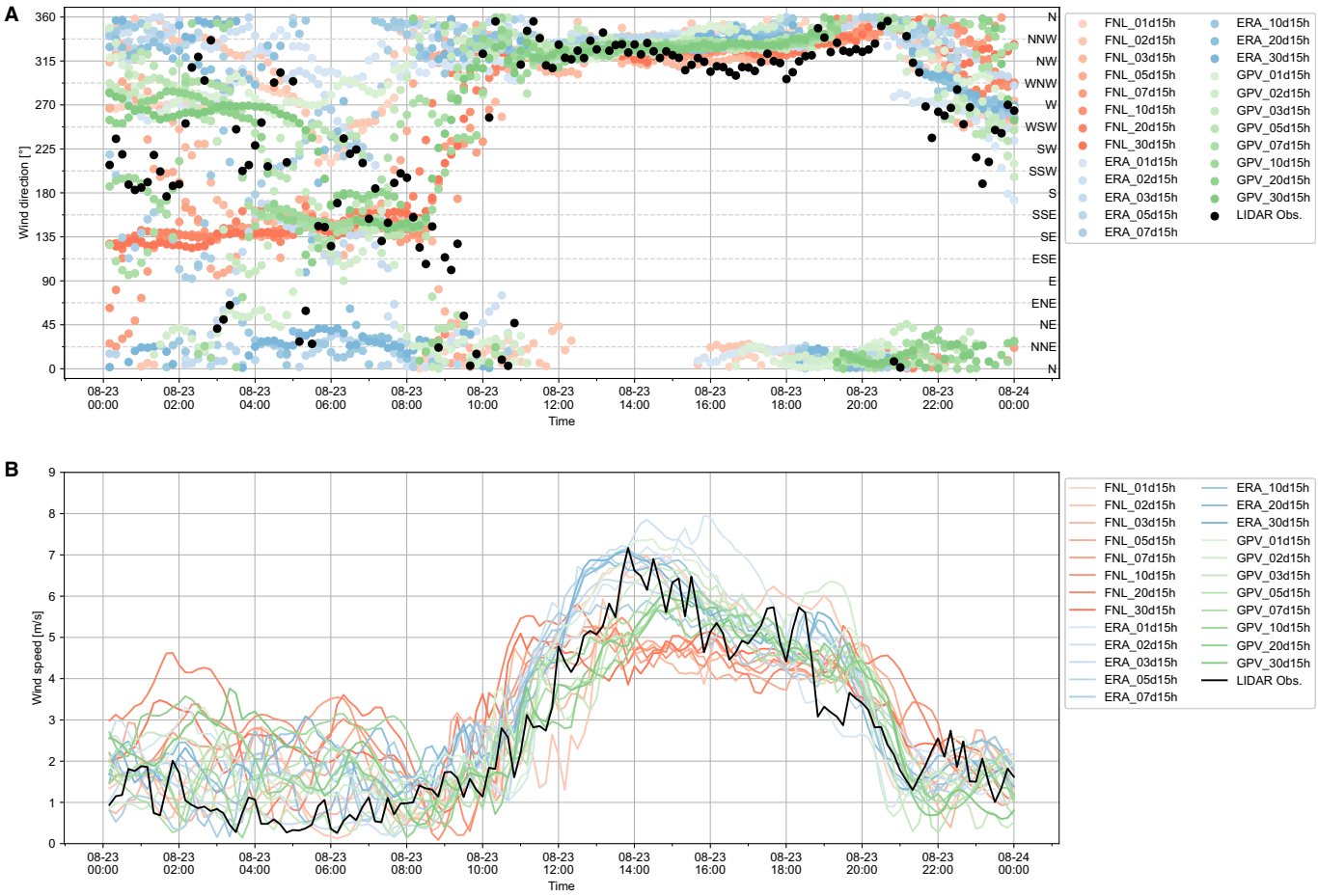

FIGURE 3. Wind direction and speed at Ohashi observation point (88 m above ground level) on August 23

3.2.2 Flow fields on 11 September 2015

Figure 5 shows the daily variation of the observed and calculated values for wind direction and wind speed (at a height of 88 m above ground level) on 11 Sept 2015. The mean height of the WRF model was 83.6 m. On this target day, the reproduction accuracies deteriorated when the calculation period exceeded 05d15h. On 23 August, the observed wind direction was unstable until the sea breeze entered; however, in the reproduction calculations, the dark-colored points with long calculation periods were concentrated in the north-west to north directions, resulting in a significantly less accurate reproduction. Similarly, almost all calculations resulted in an overestimation of the wind speed. In particular, at 05d15h, where the reproduction accuracy was the lowest, errors exceeding

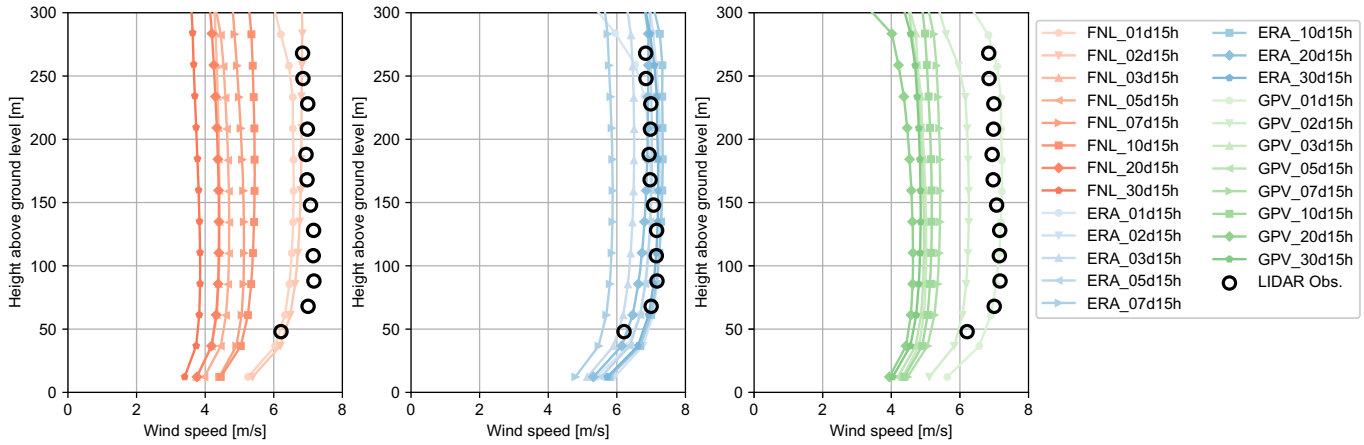

FIGURE 4. Vertical profiles of wind speed at the Ohashi observation point at 13:50 on August 23

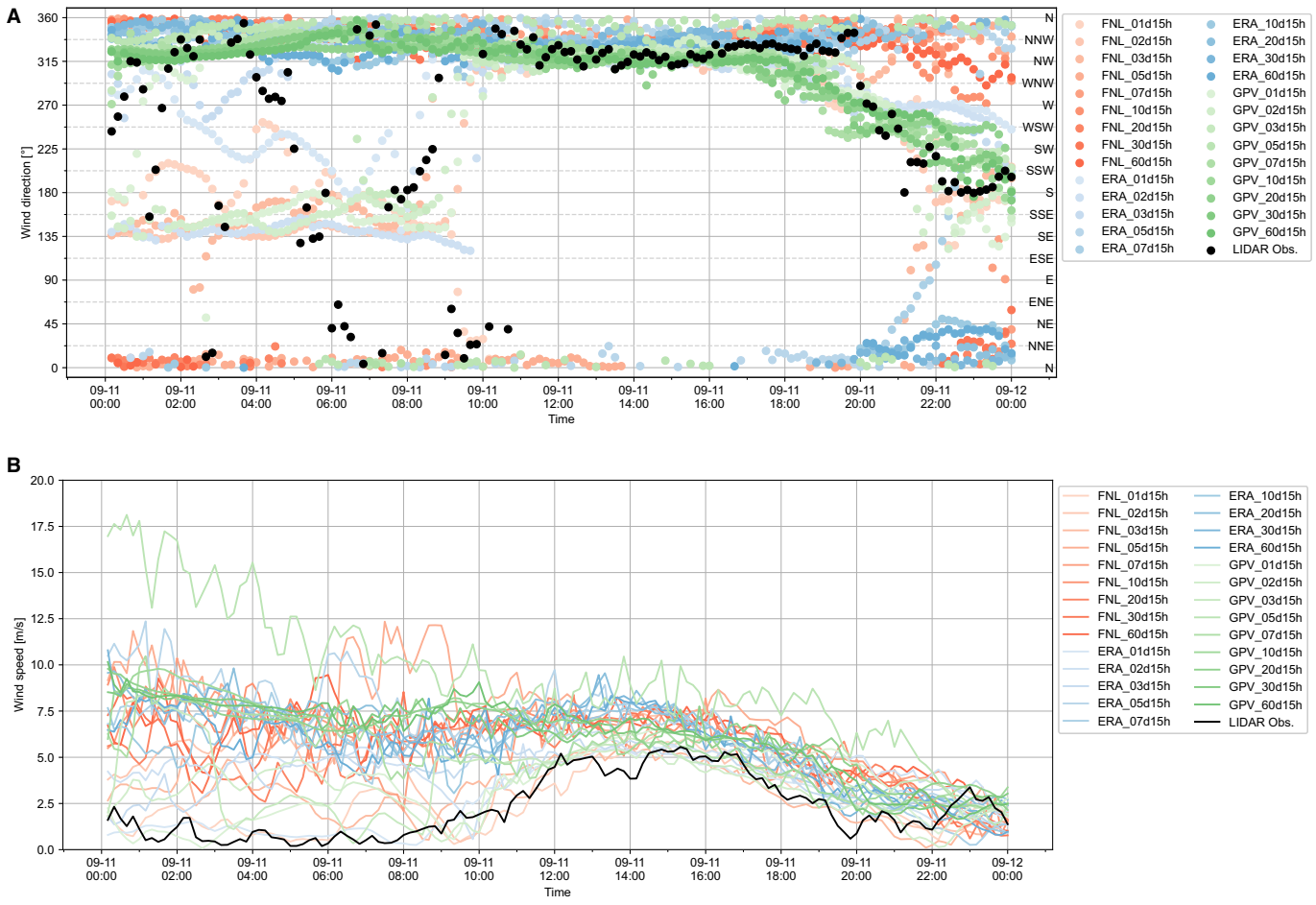

FIGURE 5. Wind direction and speed at Ohashi observation point (88 m above ground level) on September 11

10 m/s were often observed, with GPV_05d15h having a maximum error of 16.85 m/s. Observations showed that the wind direction stabilized in the northwest direction after 11:00, and the wind speed exceeded 2.5 m/s, which could be regarded as sea breezes entering the area; this trend continued until 19:10. The calculations generally reproduced the wind direction following the entry of the sea breeze; however, the wind speed was overestimated in almost all calculations.

For 23 August, the vertical profile of the wind speed is shown in Figure 6 for 15:20, when the daily maximum wind speed (as observed by Doppler LIDAR at 88 m above ground level) was 5.42 m/s. The calculations for all of the objective

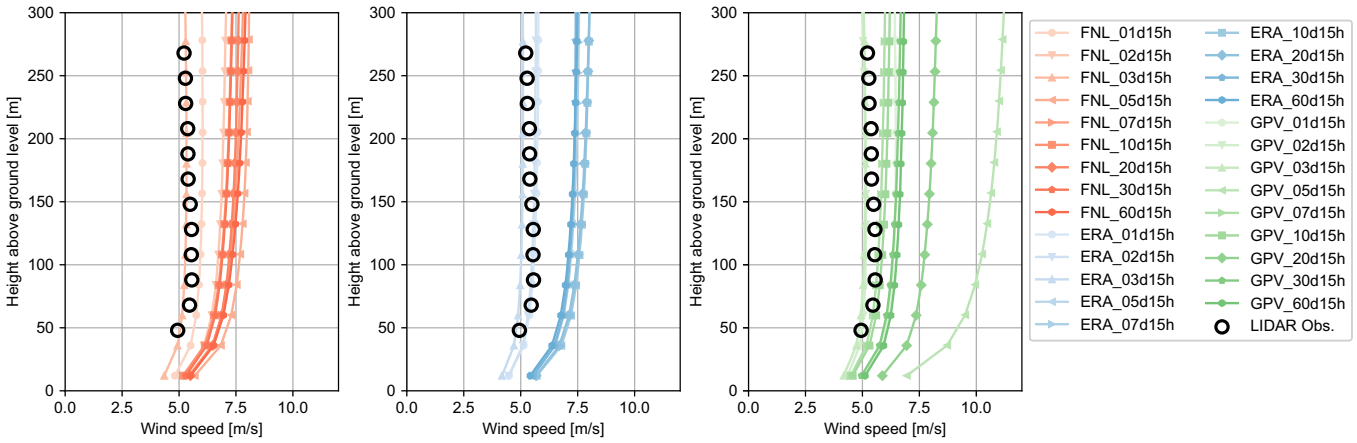

FIGURE 6. Vertical profiles of wind speed at the Ohashi observation point at 15:20 on September 11

analysis data showed good correspondence with the observed values for the calculation period from 01d15h to 03d15h; however, a tendency to overestimate wind speeds beyond 05d15h was observed, especially for GPV_05d15h. Similar to the 23 August results, the results obtained using the ERA showed the smallest variation between calculation periods.

3.3 Trial of ensemble average

In the previous sections, the results of each calculation were compared with the observed results. The accuracy of a single calculation result is deterministic; however, ensemble forecasting is used in the fields of weather and climate, where probabilistic treatment is used to reduce uncertainty. For example, in future projections of climate change, model ensembles are applied to reduce the uncertainty of individual models using the results of various global climate model projections generated by the Coupled Model Intercomparison Project (CMIP). Ensemble weather forecasts were used to reduce the uncertainty of the initial conditions, and the JMA started meso-ensemble forecasts on 27 June, 2019. A simple ensemble forecasting method used to reduce uncertainty in initial conditions is the lagged average forecasting (LAF) method.[29] In this method, initial conditions are created from objective analysis data at different times, calculations are performed, and the data are statistically treated as ensemble members for the assessment period under consideration. Generally, in the LAF method, the calculation start time is staggered regularly in terms of the time intervals and days in the objective analysis data. However, in this study, the calculation start time intervals were irregular and the short-, medium-, and long-range calculations were mixed; hence, the validity of the method as an ensemble member is not fully verified. However, an evaluation was attempted by determining the mean value and standard deviation, using the results of the reproduction calculations for different calculation periods.

Figure 7 shows the observed and averaged calculated wind speeds at 88 m above ground level on 23 August. Averages were calculated for each objective analysis. For the calculated values, the solid line shows the average of the eight cases under different calculation periods for each objective analysis data, and the colored range shows the standard deviation at each time. Similarly, Figure 8 shows the observed and averaged calculated wind speeds 88 m above ground level on 11 September. However, this is the mean and standard deviation of the nine cases under different calculation periods. The number of ensemble members differs, although the appropriate

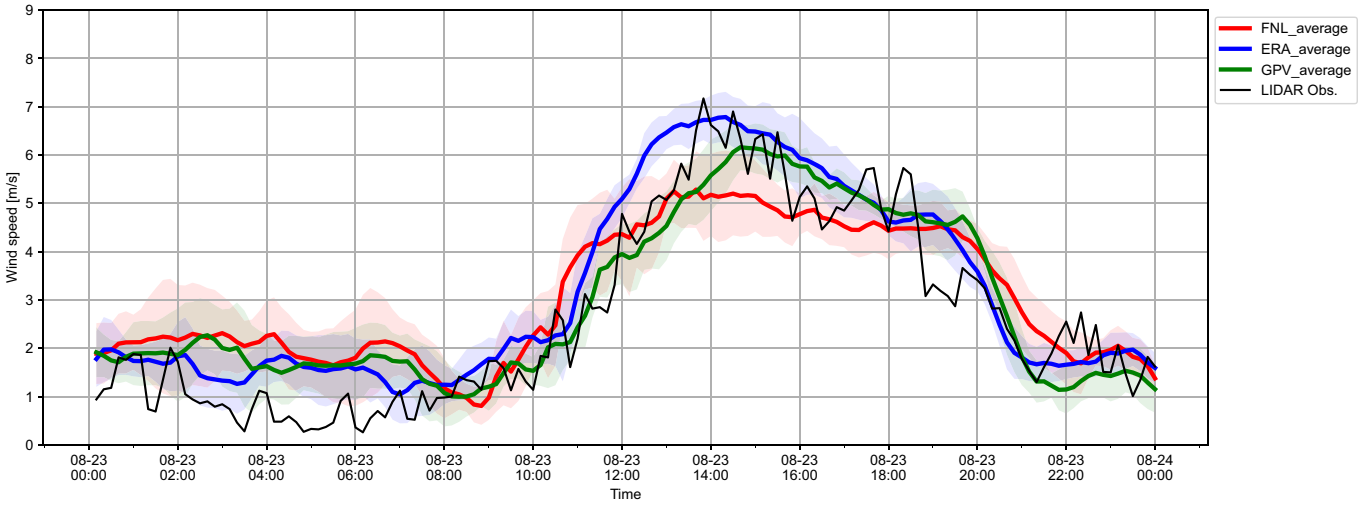

FIGURE 7. Average wind speed at Ohashi observation point (88 m above ground level) on August 23

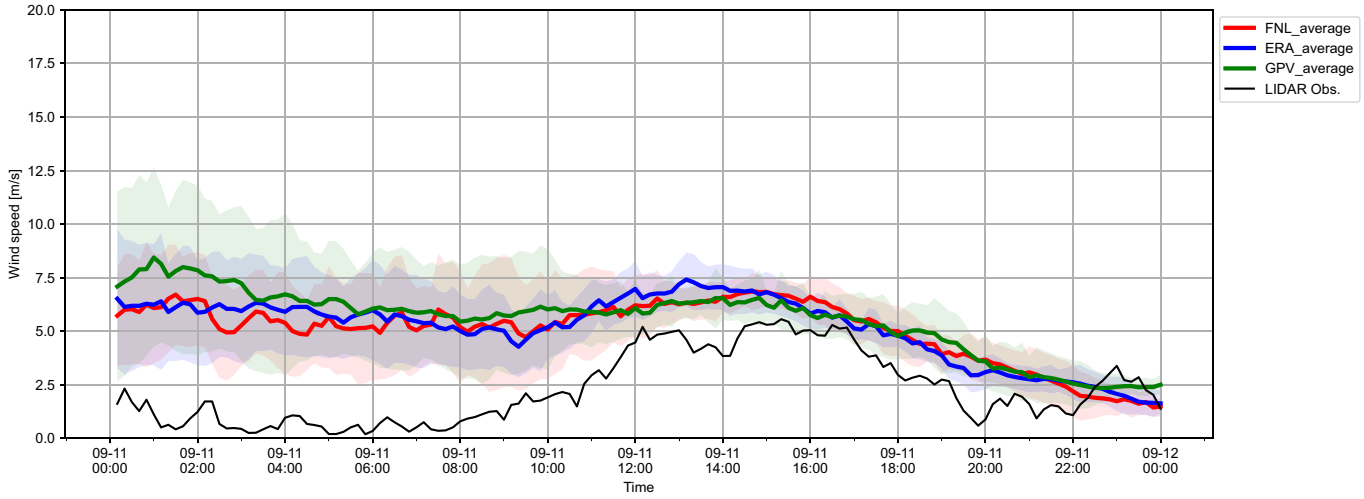

FIGURE 8. Average wind speed at Ohashi observation point (88 m above ground level) on September 11

number of ensemble members for reproduction calculations will be discussed in the future.

For 11 September, the significantly reduced accuracy of reproduction after 05d15h and the increased number of members after 05d15h means that the mean wind speeds before sea breeze entry show no improvement and have a large standard deviation. In addition, because the average wind speed was higher before the sea breeze entry was observed, the results for all objective analysis data failed to correctly capture the timing of the sea breeze entry; however, the results do show that the standard deviation decreased after sea breeze entry. In contrast, on 23 August, the short-term wind speed fluctuations in the individual calculation results were offset by averaging, and the trend of daily changes in wind speed became clear. At the time considered in the observations to mark the entry of the sea breeze, the wind speed increased by 1.47 m/s between 11:50 and 12:00, the largest daily change in wind speed within a 10-min period. The daily maximum of the 10-min wind speed change in the averaged calculation results was 10:40 for FNL, 11:00 for ERA, and 11:30 for GPV, which indicates the time of sea breeze entry in the ensemble-averaged reproduction calculations. Similarly, looking at the daily maximum wind speed change over a 10-min period for each of the individual calculations, we see cases where the maximum appeared in the early morning or afternoon. Despite the fact that the ensemble member settings for the LAF method were not fully considered, the trend of daily wind speed change was generally captured; thus, further studies will be conducted in the future, including methods for setting appropriate ensemble members.

Figure 9 shows a Taylor Diagram[30] of the observed wind speeds at 88 m above ground level for each target day and the results of the WRF reproduction calculations. The WRF calculations were for the fourth layer above ground level, and the average height for each target day was 85.5 m on 11 August, 84.7 m on 15 August, 85.0 m on 23 August, and 83.6 m on 11 September. A Taylor diagram was used to assess the reproducibility of the numerical forecast models. The distance from the origin denotes the normalized standard deviation of the forecast divided by the standard deviation of the observations. The cosine of the angle between the horizontal axes denotes the correlation coefficient between the forecasted and observed values. Therefore, the position where the normalized standard deviation and correlation coefficient are both 1 denotes the observed value. The distance from the point denoting the observed value indicates the magnitude of the RMSE (centered RMSE) of the forecasted and observed values, centered by the mean value but divided by the standard deviation of the observed ones [Note 3]. The plots denoted by ● are the results of the individual calculations, with the line connecting each symbol in the order of the calculation period. The plots shown in ■ denote the average results for each objective analysis data point. Some calculation results for 11 September, 2015 exceeded the display range of the Taylor diagram; in such cases, the values of the centered RMSE (upper row) and correlation coefficient (lower row) are shown at the bottom of the diagram. Note that the centered RMSE was divided by the standard deviation of the observed values; hence, the centered RMSEs for different target dates cannot be compared in the diagram.

The Taylor diagram for 11 August shows that the averaged result of the centered RMSE was the smallest for all objective analysis data; for the correlation coefficient, the averaged result was largest for FNL, third largest for ERA, and the second largest for GPV. The correlation coefficient and centered RMSE results for GPV_01d15h (which has the shortest calculation period in GPV) are not necessarily good, indicating that it is not possible to simply determine the analysis accuracy from the length of the calculation period.

For 15 and 23 August, the averaged results were also generally good for both the correlation coefficient and centered RMSE. In particular, the results using the ERA on 23 August showed that the differences in the correlation coefficient and centered RMSE between the individual cases were small, and the averaged results were optimal, with the largest correlation coefficient and smallest centered RMSE. On the other hand, on 11 September, the accuracy of the analysis was extremely low at 05d15h, as indicated by 4 on the Taylor diagram; furthermore, the accuracy of the analysis was also low for cases beyond 05d15h. More cases were present as ensemble members beyond 05d15h; hence, no improvement was achieved in the analysis accuracy obtained via ensemble averaging.

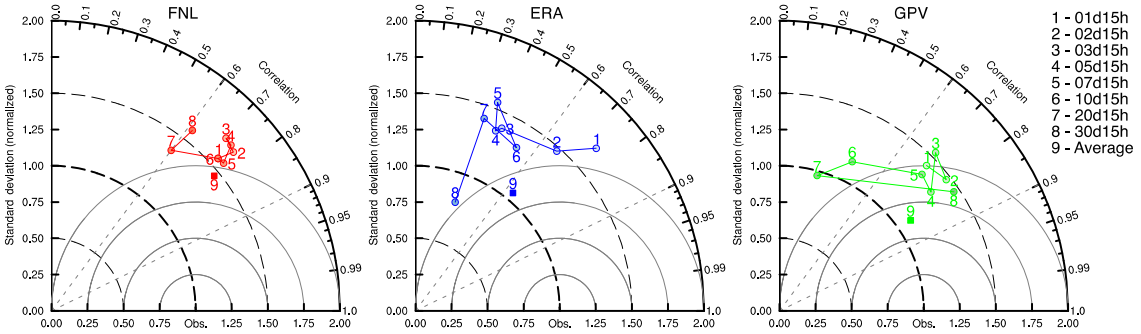

A August 11, 2015

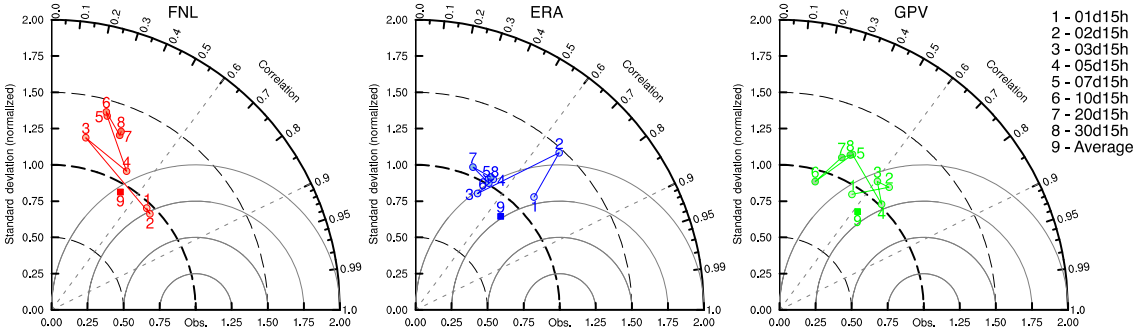

B August 15, 2015

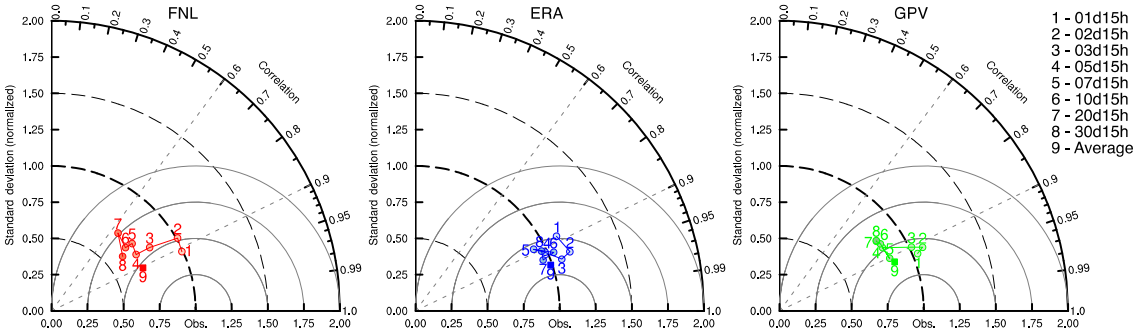

C August 23, 2015

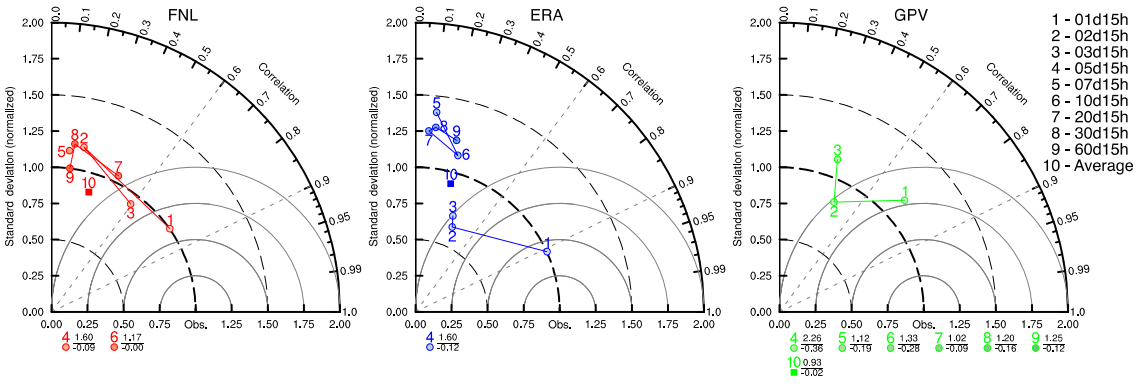

D September 11, 2015.

FIGURE 9. Taylor diagram for the wind speed simulation results

4. Conclusion

The influence of initial and boundary condition settings upon the reproduction accuracy of the flow field over the city was investigated using a meso-scale numerical weather prediction model. As a method of investigation, initial and boundary conditions derived from different objective analysis data were applied, the length of spin-up calculation up to the evaluation target date was varied, and reproduction calculations were performed for four target days on 11 August, 2015; 15 August, 2015; 23 August, 2015; and 11 September, 2015. The results were compared with surface observations obtained by the Fukuoka District Meteorological Observatory as well as upper-air observations of the flow field obtained using Doppler LIDAR at the Ohashi Campus of Kyushu University.

By comparison of the sea-level pressure and wind speed against surface observations, the influence of the different spin-up calculation periods upon the reproduction accuracy was shown; this can be attributed to the initial conditions of the pressure field. In particular, when typhoons and developing cyclones were included in the initial conditions and the calculation period was short (i.e., a few days), the reproducibility of the pressure field had a significant impact upon the reproducibility of the flow field, and the reproducibility of the day under evaluation may have decreased significantly. There was also a concern that the accuracy might decrease as the aided calculation period became longer, though this was not generally the case. In a study comparing the forecast errors of 3-day, 5-day, and 7-day forecasts in JMA's global spectral model, it was reported that in some cases, the errors were smaller for 7-day forecasts than for 5-day ones,[31] and the errors did not necessarily increase linearly with the calculation period. The influence of atmospheric conditions upon the reproducibility of the results of this study was considered to have had a greater impact than the calculation period. No clear trend was observed in the differences between the objective analysis data and surface observations.

The results for 11 September (which had the poorest reproducibility when compared against surface observations) and 23 August (which had the best reproducibility) were compared with wind direction and wind speed observations obtained using Doppler LIDAR. In particular, reproducibility was significantly lower in cases where the initial conditions included a low-pressure system passing over northern Kyushu or a typhoon. However, the wind direction was generally reproduced once the sea breeze entered the area. On 23 August, the accuracy of the reproduced wind direction was low during the period prior to sea breeze entry; however, when the wind direction was unstable and the wind speed low, both wind direction and wind speed were generally reproduced after sea breeze entry. The vertical profiles of wind speed at the time of the daily maximum sea breeze wind speed for both days showed a tendency to under- and over-estimate the wind speed as the spin-up calculation became longer on 23 August and 11 September, respectively. In terms of the differences between the objective analysis data, the smallest variation in wind speed was observed when using ECMWF ERA-Interim.

Based on the above considerations, the LAF method (which reduces the uncertainty of the initial conditions by shifting the calculation start time) was adopted, because the deterministic approach (which discusses accuracy using a single calculation result) is limited. In the present study, the calculation start time intervals were irregular, and the short, medium, and long-range calculations were mixed; thus, the validity of the method as an ensemble member has not been fully verified. Nevertheless, on certain target dates where little variation occurred in the reconstruction accuracy (owing to the length of the aided calculations), the ensemble-averaged reconstructions showed good correspondence with the observations. In the future, the method of setting the ensemble members and the number of ensemble members will be examined.

Acknowledgments

This work was supported by JSPS KAKENHI (grant number JP20K21035). The authors would like to express their special thanks to the funding sources. The computation was performed using the computer resources offered under the category of General Projects by the Research Institute for Information Technology, Kyushu University.

Disclosure

The authors have no conflict of interest.

Data availability statement

The data supporting the findings of this study are openly available at GitHub, at https://github.com/yoichi-kawamoto/lidar-wrf-comparison.

Endnotes

Note 1) The η coordinate is defined as

$$\eta = \frac{p_h - p_{ht}}{p_{hs} - p_{ht}}, \tag{1}$$

where p_h is the hydrostatic pressure at a certain altitude, p_{hs} is the hydrostatic pressure at the ground surface, and p_{ht} is the hydrostatic pressure at the top of the model; these have fixed values in the WRF model. Therefore, η was 1 at the ground surface and 0 at the top of the model.

Note 2) As the name ERA-Interim suggests, this is a provisional version. ERA5, with a spatial resolution of 30 km and time interval of one hour, has now been made available.

Note 3) For the predicted values f_n and observed values r_n (for sample size N), the respective standard deviations σ_f and σ_r are defined as

$$\sigma_f = \sqrt{\frac{1}{N}\sum_{n=1}^{N}\left(f_n - \overline{f}\right)^2}, \tag{2}$$

$$\sigma_r = \sqrt{\frac{1}{N}\sum_{n=1}^{N}\left(r_n - \overline{r}\right)^2}, \tag{3}$$

where $\overline{f}$ and $\overline{r}$ denote the mean of the predictions and observations, respectively. The correlation coefficient R between the predictions and observations is defined by the following equation:

$$R = \frac{\frac{1}{N}\sum_{n=1}^{N}\left(f_n - \overline{f}\right)\left(r_n - \overline{r}\right)}{\sigma_f \sigma_r}. \tag{4}$$

In the case of time-series data, R indicates similarity in the patterns of change. Mean error (ME) was used as a measure of systematic bias in the predictions. The mean error is also referred to as bias. The mean error or bias $\overline{E}$ was defined using

$$\overline{E} = \frac{1}{N}\sum_{n=1}^{N}\left(f_n - r_n\right) = \overline{f} - \overline{r}. \tag{5}$$

The root mean square error (RMSE) E is used as a measure of the standard magnitude of the prediction error; it is defined as

$$E = \sqrt{\frac{1}{N}\sum_{n=1}^{N}\left(f_n - r_n\right)^2}. \tag{6}$$

The centered RMSE E', which is calculated using the averages of the predicted values f_n and observed values r_n, is defined as follows:

$$E' = \sqrt{\frac{1}{N}\sum_{n=1}^{N}\left[\left(f_n - \overline{f}\right) - \left(r_n - \overline{r}\right)\right]^2} = \sqrt{\frac{1}{N}\sum_{n=1}^{N}\left(f_n - r_n - \overline{E}\right)^2}. \quad (7)$$

Therefore, the relationship between the RMSE (E), ME ($\overline{E}$), and centered RMSE (E') is as follows:

$$E^2 = \overline{E}^2 + E'^2. \quad (8)$$

The Taylor diagram is a two-dimensional plot of the correlation coefficient between the predicted and observed values (R), centered RMSE (E'), and standard deviation (σ_f, σ_r). The relationships are

$$E'^2 = {\sigma_f}^2 + {\sigma_r}^2 - 2\sigma_f\sigma_r R. \quad (9)$$

Equation 9 shares similarities with the law of cosines

$$c^2 = a^2 + b^2 - 2ab\cos\phi. \quad (10)$$

This is an overview of the Taylor Diagram.

References

1 Mochida A, Murakami S, Ojima T, Kim S, Ooka R, Sugiyama H. CFD analysis of mesoscale climate in the greater Tokyo area. *J Wind Eng Ind Aerodyn*. 1997;**67–68**:459–477. 10.1016/S0167-6105(97)00060-3.

2 Kwok YT, Ng EYY. Trends, topics, and lessons learnt from real case studies using mesoscale atmospheric models for urban climate applications in 2000–2019. *Urban Clim*. 2021;**36**:100785. 10.1016/j.uclim.2021.100785.

3 Grell GA, Dudhia J, Stauffer D. A description of the fifth-generation Penn State/NCAR mesoscale model (MM5), NCAR technical notes. *Univ Corp Atmos Res*. 1994;1–121. 10.5065/D60Z716B.

4 Skamarock WC, Klemp JB, Dudhia J, et al. A description of the advanced research WRF version 3, NCAR technical notes. *Univ Corp Atmos Res*. 2008;**6**:1–113. 10.5065/D68S4MVH.

5 Kawamoto Y, Ooka R. Improvement of parameterization of ground surface and incorporation of anthropogenic heat release - development of urban climate analysis model using MM5 part 1, *J Environ Eng (Transactions of AIJ)*. 2008;**73**(631):1125–1132 (in Japanese).

6 Kawamoto Y, Ooka R. Incorporating an urban canopy model to represent the effect of buildings - development of urban climate analysis model using MM5 part 2, *J Environ Eng (Transactions of AIJ)*. 2009;**74**(642):1009–1018. (in Japanese).

7 Ooka R, Sato T, Harayama K, Murakami S, Kawamoto Y. Thermal energy balance analysis of the Tokyo metropolitan area using a mesoscale meteorological model incorporating an urban canopy model, *Boundary-Layer Meteorol*. 2011;**138**:77–97. 10.1007/s10546-010-9550-8.

8 Kawamoto Y, Yoshikado H, Ooka R, Hayami H, Hong H, Khiem MV. *Sea Breeze Blowing into Urban Areas: Mitigation of the Urban Heat Island Phenomenon, 2nd Chapter of Ventilating Cities*. Dordrecht, Nederland: Springer Geography; 2012; 11–32. 10.1007/978-94-007-2771-7_2.

9 Kawamoto Y. Effect of urbanization on the urban heat Island in Fukuoka-Kitakyushu metropolitan area, Japan. *Procedia Eng*. 2016;**169**:224–231. 10.1016/j.proeng.2016.10.027.

10 Kawamoto Y. Effect of land-use change on the urban heat Island in the Fukuoka–Kitakyushu metropolitan area, Japan. *Sustainability*. 2017;**9**(9):16. 10.3390/su9091521.

11 Lorenz EN. Deterministic nonperiodic flow. *J Atmos Sci*. 1963;**20**(2):130–141. 10.1175/1520-0469(1963)020<0130:DNF>2.0.CO;2.

12 Lorenz EN. The predictability of hydrodynamic flow. *Trans NY Acad Sci*. 1963;**25**(4):409–432.

13 Lorenz EN. (Writer), Sugiyama M, Sugiyama T. (translator). The essence of chaos, Kyoritsu Shuppan. 1997 (in Japanese).

14 Skamarock WC. Evaluating mesoscale NWP models using kinetic energy spectra. *Mon Weather Rev*. 2004;**132**(12):3019–3032. 10.1175/MWR2830.1.

15 Jerez S, López-Romero JM, Turco M, et al. On the spin-up period in WRF simulations over Europe: trade-offs between length and seasonality, *J Adv Model Earth Syst*. 2020;**12**(4). 10.1029/2019MS001945.

16 Kawamoto Y. Investigation into the uncertainty of initial and boundary conditions for meso-scale numerical analysis. *Summaries of Technical Papers of Annual Meeting, Architectural Institute of Japan, Environmental Engineering-I*. Tokyo, Japan: Architectural Institute of Japan; 2017:683–684 (in Japanese).

17 Kawamoto Y. Investigation into the uncertainty of initial and boundary conditions for meso-scale numerical analysis, Part 2, Evaluations of analytical error. *Summaries of Technical Papers of Annual Meeting, Architectural Institute of Japan, Environmental Engineering-I*. Tokyo, Japan: Architectural Institute of Japan; 2019:831–832 (in Japanese).

18 Kawamoto Y. Investigation into the uncertainty of initial and boundary conditions for meso-scale numerical analysis, Part 3 Comparison with doppler LIDAR observation. *Summaries of Technical Papers of Annual Meeting, Architectural Institute of Japan, Environmental Engineering*. Tokyo, Japan: Architectural Institute of Japan. 2021:2049–2050. (in Japanese).

19 Thompson G, Field PR, Rasmussen RM, Hall WD. Explicit forecasts of winter precipitation using an improved bulk microphysics scheme. Part II: implementation of a new snow parameterization, *Mon Weather Rev*. 2008;**136**(12):5095–5115. 10.1175/2008MWR2387.1.

20 Mlawer EJ, Taubman SJ, Brown PD, Iacono MJ, Clough SA. Radiative transfer for inhomogeneous atmosphere: RRTM, a validated correlated-k model for the longwave, *J Geophy Res*. 1997;**102**(D14):16663–16682. 10.1029/97JD00237.

21 Chou MD, Suarez MJ, Liang XZ, Yan MMH. A thermal infrared radiation parameterization for atmospheric studies. *NASA Technical Report Series on Global Modeling and Data Assimilation*. Maryland, USA: National Aeronautics and Space Administration: 2001;**19**:68.

22 Janjic ZI. The Step-Mountain eta coordinate model: further developments of the convection, viscous sublayer, and turbulence closure schemes, *Mon Weather Rev*. 1994;**122**(5):927–945. 10.1175/1520-0493(1994)122<0927:TSMECM>2.0.CO;2.

23 Tewari M, Chen F, Wang W, et al. Implementation and verification of the unified NOAH land surface model in the WRF model. 20th Conference on Weather Analysis and Forecasting/16th Conference on Numerical Weather Prediction, Seattle, U.S. 2004.

24 Grell GA, Devenyi D. A generalized approach to parameterizing convection combining ensemble and data assimilation techniques. *Geophys Res Lett*. 2002;**29**(14):38-1–38-4. 10.1029/2002GL015311.

25 *Fukuoka City: Hakatakouwankeikaku (Hakata port project)*, Fukuoka, Japan: Fukuoka city; 2016. (in Japanese).

26 National Centers for Environmental Prediction/National Weather Service/NOAA/U.S. Department of Commerce. NCEP GDAS/FNL 0.25 degree global tropospheric analyses and forecast grids, research data archive at the National Center for Atmospheric Research, Computational and Information Systems Laboratory. Accessed 2021. 10. 1. 10.5065/D65Q4T4Z.

27 Dee DP, Uppala SM, Simmons AJ, et al. The ERA-interim reanalysis: configuration and performance of the data assimilation system, *Q J R Meteorol Soc*. 2011;**137**(656):553–597. 10.1002/qj.828.

28 Davies HC, Turner RE. Updating prediction models by dynamical relaxation: an examination of the technique. *Q J R Meteorol Soc*. 1977;**103**(436):225–245. 10.1002/qj.49710343602.

29 Hoffman RN, Kalnay E. Lagged average forecasting, an alternative to Monte Carlo forecasting. *Tellus A*. 1983;**35A**(2):100–118. 10.1111/j.1600-0870.1983.tb00189.x.

30 Taylor KE. Summarizing multiple aspects of model performance in a single diagram. *J Geophys Res*. 2001;**106**(D7):7183–7192. 10.1029/2000JD900719.

31 Kimoto M, Mukougawa H, Yoden S. Medium-range forecast skill variation and blocking transition. A case study. *Mon Weather Rev*. 1992;**120**(8):1616–1627. 10.1175/1520-0493(1992)120<1616:MRFSVA>2.0.CO;2.

How to cite this article: Kawamoto Y. Investigation of the uncertainty of initial and boundary conditions in the hindcasts of flow fields over urban areas using a mesoscale numerical weather prediction model. *Jpn Archit Rev*. 2022;5:517–529. https://doi.org/10.1002/2475-8876.12282